Assessing dynamic metabolic heterogeneity in non-small cell lung cancer patients via ultra-high sensitivity total-body [18F]FDG PET/CT imaging: quantitative analysis of [18F]FDG uptake in primary tumors and metastatic lymph nodes

DaQuan Wang[1] · Xu Zhang[2] · Hui Liu[3] · Bo Qiu[1] · SongRan Liu[4] · ChaoJie Zheng[3] · Jia Fu[4] · YiWen Mo[2] · NaiBin Chen[1] · Rui Zhou[1] · Chu Chu[1] · FangJie Liu[1] · JinYu Guo[1] · Yin Zhou[5] · Yun Zhou[3] · Wei Fan[2] · Hui Liu[1]

Abstract

Purpose This study aimed to quantitatively assess [18F]FDG uptake in primary tumor (PT) and metastatic lymph node (mLN) in newly diagnosed non-small cell lung cancer (NSCLC) using the total-body [18F]FDG PET/CT and to characterize the dynamic metabolic heterogeneity of NSCLC.

Methods The 60-min dynamic total-body [18F]FDG PET/CT was performed before treatment. The PTs and mLNs were manually delineated. An unsupervised K-means classification method was used to cluster patients based on the imaging features of PTs. The metabolic features, including Patlak-Ki, Patlak-Intercept, SUV_{mean}, metabolic tumor volume (MTV), total lesion glycolysis (TLG), and textural features, were extracted from PTs and mLNs. The targeted next-generation sequencing of tumor-associated genes was performed. The expression of Ki67, CD3, CD8, CD34, CD68, and CD163 in PTs was determined by immunohistochemistry.

Results A total of 30 patients with stage IIIA–IV NSCLC were enrolled. Patients were divided into fast dynamic FDG metabolic group (F-DFM) and slow dynamic FDG metabolic group (S-DFM) by the unsupervised K-means classification of PTs. The F-DFM group showed significantly higher Patlak-Ki ($P < 0.001$) and SUV_{mean} ($P < 0.001$) of PTs compared with the S-DFM group, while no significant difference was observed in Patlak-Ki and SUV_{mean} of mLNs between the two groups. The texture analysis indicated that PTs in the S-DFM group were more heterogeneous in FDG uptake than those in the F-DFM group. Higher T cells (CD3+/CD8+) and macrophages (CD68+/CD163+) infiltration in the PTs were observed in the F-DFM group. No significant difference was observed in tumor mutational burden between the two groups.

Conclusion The dynamic total-body [18F]FDG PET/CT stratified NSCLC patients into the F-DFM and S-DFM groups, based on Patlak-Ki and SUV_{mean} of PTs. PTs in the F-DFM group seemed to be more homogenous in terms of [18F]FDG uptake than those in the S-DFM group. The higher infiltrations of T cells and macrophages were observed in the F-DFM group, which suggested a potential benefit from immunotherapy.

Keywords Dynamic total-body PET · [18F]FDG · Metabolic heterogeneity · Lung cancer

DaQuan Wang, Xu Zhang, Hui Liu, Bo Qiu and SongRan Liu contributed equally to the study.

✉ Wei Fan
  fanwei@sysucc.org.cn

✉ Hui Liu
  liuhuisysucc@126.com

Extended author information available on the last page of the article

Introduction

Non-small cell lung cancer (NSCLC) represents the largest entity of lung cancer. Although the combination of immunotherapy with surgery, chemotherapy, and radiotherapy has led to a remarkable improvement in the prognosis of NSCLC patients, a noticeable proportion of patients fail to be cured due to tumor heterogeneity [1]. In addition to the tumor, node, and metastasis (TNM) stage, tumor heterogeneity assessed by imaging and histopathologic

examination has been confirmed to be associated with the prognosis of patients [2–4]. [18F]fluorodeoxyglucose positron emission tomography/computed tomography ([18F]FDG PET/CT) plays a significant role in the diagnosis and assessment of tumor heterogeneity because of its noninvasive property [5]. Heterogeneities in [18F]FDG uptake are observed in both primary tumors (PTs) and metastatic lymph nodes (mLNs) in lung cancer patients[6, 7]. Previous studies suggested that the intratumoral heterogeneity of FDG uptake was predictive of treatment response and prognosis in various tumors [8, 9], including non-small cell lung cancer [10–12].

Different imaging modalities, such as dynamic contrast-enhanced magnetic resonance imaging (DCE-MRI) and 1-h dynamic [18F]FDG PET/CT, have yielded kinetic parameters reflecting tumor heterogeneity. A full 1-h dynamic [18F]FDG PET acquisition allows tumor blood flow and metabolism evaluation after a single injection of [18F]FDG. Recently, an investigation of tumor heterogeneity using texture analysis has emerged. Standard PET/CT parameters combined with texture analysis provide useful information for clarifying the correlation between metabolic heterogeneity and histological types, tumor aggressiveness, or patient prognosis [13–15]. Likewise, the present study hypothesizes that dynamic FDG uptake patterns of PTs and mLNs assessed by total-body [18F]FDG PET/CT might also bring valuable information for a deeper insight into tumor heterogeneity.

The clinically widely used PET scanners, which are short axial field-of-view (AFOV), have some limitations, including a long scanning time, a low signal-to-noise ratio (SNR), a high dose of ionizing radiation, and most importantly the lack of whole-body quantitative imaging. Total-body PET scanner was developed to overcome these limitations. It provides a 1940-mm scan range to cover the entire human body. In addition, the markedly increased sensitivity is obtained by increasing the number of detectors, which allows for the total-body dynamic acquisition and improves the detectability of exiguous changes [16]. Compared with conventional PET, a total-body PET scanner provides new opportunities for a more accurate tracer kinetic analysis with higher spatial resolution [17]. Moreover, the Patlak-Ki extracted from dynamic total-body PET represents the rate of FDG uptake and is an absolute quantitative index of FDG metabolism, which separates the metabolized FDG from FDG uptake and provides a more accurate characterization of tumor metabolic heterogeneity [18].

This study aimed to quantitatively assess [18F]FDG uptake in PTs and mLNs in newly diagnosed NSCLC patients using the total-body [18F]FDG PET/CT and to characterize the dynamic metabolic heterogeneity of NSCLC.

Methods

Patients and study design

Patients with stage IIIA–IV NSCLC were enrolled in the present study. Eligible patients were required to meet the following criteria: (1) untreated histologically or cytologically confirmed NSCLC; (2) patients aged between 18 and 75 years; (3) patients with unresectable stage IIIA–IV disease according to the 8th edition of the American Joint Committee on Cancer Staging System; (4) Eastern Cooperative Oncology Group (ECOG) Performance Status score of 0 or 1; (5) life expectancy $\geq$ 12 weeks; (6) adequate hematologic, renal, and hepatic functions: absolute neutrophil count $\geq$ 1500/uL, hemoglobin $\geq$ 9.0 mg/dL, platelet $\geq$ 100,000/uL, serum creatinine clearance $\geq$ 50 ml/min, serum bilirubin $\leq$ 1.5 times the upper limit of normal (ULN), and aspartate transaminase and alanine transferase $\leq$ 2.5 times the ULN; and (7) forced expiratory volume in 1 s (FEV_1) $\geq$ 0.8 L.

Exclusion criteria included history of another primary malignancy, uncontrolled intercurrent illness, pregnant or breastfeeding women, and any situation that would be improper for this study judged by researchers.

Before treatment, all patients underwent both total-body [18F]FDG PET/CT dynamic scan and delayed static PET/CT scan on the uEXPLORER PET/CT scanner (United Imaging Healthcare, Shanghai, China). Patients with a high blood glucose level (> 10 mmol/l) or those who were unable or unwilling to undergo a PET scan were excluded. This study was approved by the institutional review board. All patients signed a written informed consent form.

Total-body [18F]FDG PET/CT imaging

The total-body [18F]FDG PET/CT imaging protocol is described in Supplementary Fig. 1. Patients were required to avoid strenuous exercise 24 h beforehand and fast for up to 6 h prior to the total-body [18F]FDG PET/CT scan. At the time of [18F]FDG injection, the fasting blood glucose level was required to be less than 10 mmol/L. The 60-min dynamic total-body [18F]FDG PET imaging was performed from head to toe after intravenous injection of 3.0 MBq/kg FDG via a vein near the ankle. The 10-min delayed static PET imaging was subsequently conducted 3 h after the injection (and 2 h after the conclusion of the dynamic total-body [18F]FDG PET imaging). During the interval between the dynamic and delayed static PET imaging, the patient was required to stay quiet.

Quantitative analysis of dynamic metabolic uptake

The quantitative analysis of dynamic [^{18}F]FDG uptake was shown in Supplementary Figs. 2 and 3. The dynamic acquisition was reconstructed into 92 dynamic time frames, with a spatial resolution of 1.67 mm × 1.67 mm × 2.89 mm. The dynamic time frames were as follows: 2 s (2 s) frame duration for 1–30th frame, 5 s for 31–42nd frame, 10 s for 43–48th frame, 30 s for 49–52nd frame, 60 s for 53–77th frame, and 120 s for 78–92nd frame. All time frames were reconstructed using the ordered subset expectation maximization (OSEM) (4 iterations, 20 subsets) with the point-spread function recovery and time-of-flight. Attenuation, random, and scatter corrections were applied to all time frames. The parametric images (Patlak-Ki, Patlak-Intercept) were calculated from the 20–60-min frames using the Patlak graphical analysis and an image-derived arterial input function (AIF) extracted from the descending aorta across all 92 frames from 0 to 60 min.

The CT, PET, and endobronchial ultrasound-guided biopsy were used for the diagnosis of metastatic lymph nodes (mLNs) [19]. The criteria of metastatic lymph node included: short-axis size ≥ 10 mm on pre-treatment CT scan, metastasis reported on the pre-treatment PET scan (SUV_{max} ≥ 2.5)[20], or biopsy positive on endobronchial ultrasound-guided biopsies. Volumes of interest (VOIs) of PTs and mLNs were manually delineated on the last time frame (10 min) of dynamic PET data by a nuclear medicine physician and a radiation oncologist with more than 10 years of professional experience, and a consensus was reached when there was an inconsistency. The rigid registration was performed between the PET and CT images for tumor delineation. The manual delineation of VOI was performed on PET images, with reference to the morphological structure displayed on CT images (Supplementary Fig. 4a,b). Besides, for the patients whose primary tumor and mLN were fused, the double evaluation was applied by two experts to identify the boundary between PT and mLN (Supplementary Fig. 4c,d). VOIs including the PTs and mLNs were delineated using the 3D-Slicer software (https://www.slicer.org) and Evidance Platform. The necrotic regions within the tumor were considered to be part of the tumor during delineation (Supplementary Fig. 4a,b).

Unsupervised K-means classification of PTs and mLNs

An unsupervised K-means clustering algorithm was used to classify patients into different groups. The features used for classification included the SUV_{mean} extracted from 50- to 60-min static PET images, the metabolic tumor volume (MTV), total lesion glycolysis (TLG), and the mean values of Patlak-Ki and Patlak-Intercept extracted from the Patlak parametric images. The Laplacian Score (LS), an unsupervised feature selection method, combined with a distance-based entropy measure (LSE), was used to select the optimal feature subset for clustering [21]. The LS evaluated the importance of a feature by its locality preserving ability, and a smaller LS indicated that the feature was more important. The number of clusters was determined by the silhouette coefficient, which was higher when clusters were dense and well separated. The clustering was performed using the scikit-learn package (https://scikit-learn.org). Textural features extracted from VOIs were evaluated.

Capture-based targeted next-generation sequencing of PTs

Archived formalin-fixed paraffin-embedded (FFPE) tissue samples of PTs were collected. Matched peripheral blood samples were also collected as the germline control. The genomic DNA was extracted from FFPE and peripheral blood samples. A capture probe covering 1021 genes that were correlated with carcinogenesis and tumor development was employed. The next-generation sequencing (NGS) was performed on the Next Seq 2000 Sequencing system (Illumina Inc., Chicago, IL, USA).

Immunohistochemistry and quantification of the expressions of CD3, CD8, CD68, CD163, CD34, and Ki67 in clinical specimens

Tissue blocks of FFPE samples of PTs were sectioned into 3-μm slices for immunohistochemistry (IHC). First, the presence of PTs was confirmed using hematoxylin and eosin (H&E) staining. After deparaffinization and hydration, the other serial slides were heated with ethylenediaminetetraacetic acid (EDTA, pH 8.0) in an autoclave to complete antigen retrieval. After cooling, specimens were incubated with 3% H_2O_2 at room temperature (RT) for 10 min to extinguish endogenous peroxidase activity. Sections were then incubated with the primary antibodies against CD3 (ZS; clone LN10; dilution, 1:100), CD8 (ZS; clone SP16), CD68(ZS; clone KP1), CD163 (ZS; clone 10D6), CD34 (ZS; clone 10C9), and Ki67 (ZS; clone MIB1) for 60 min at 37 ℃, and antibody dilution buffer was used to create blank control. Following thrice washing with phosphate-buffered saline (PBS; 2 min/step), an enzyme-labeled secondary antibody (ZS) was added to slices and incubated at 37 ℃ for 20 min. After another thrice washing with PBS (2 min/step), freshly prepared 3,3′-diaminobenzidine (DAB) was used as a chromogenic substrate for visualization through a 5-min incubation at RT, and sections were finally counterstained with hematoxylin.

The mean micro-vessel number of the most intensive neovascularization areas was used to define the

micro-vessel density (MVD). First, after navigating the whole slide at $40\times$ magnification, a CD34 stained hot spot was identified to further select five high-power fields (HPFs) with the highest density of CD34$^+$ micro-vessels. Finally, based on the selected HPFs, an average of CD34 + micro-vessels per HPF was calculated to define the MVD.

All slides stained with H&E containing PTs were scanned using an Aperio Scanner (Leica Biosystem, Wetzlar, Germany). Whole-slide images (WSIs) were reviewed by 2 pathologists with more than 5 years of professional experience in telepathology. The number of WSIs per case ranged from one to five.

Two pathologists with more than 5 years of professional experience, who were blinded to clinical data, were employed to confirm IHC quality, calculate MVD, and assist in the pre-training of machine learning, in which any disagreement was discussed until a consensus was reached. CD3$^+$ tumor-infiltrating lymphocyte (TIL), CD8$^+$ TIL, CD68$^+$ tumor-associated macrophage (TAM), CD163$^+$ TAM, and Ki67 were computed using the digital image analysis (DIA) via PathoImpression software on the Evidance Platform.

Statistical analysis

The comparisons of image-derived PET metrics and IHC indices between clustered groups were performed using the independent-samples t-test or the Mann–Whitney U test according to the normality of the variables. $P < 0.05$ was considered statistically significant. The Bonferroni correction was applied for multiple comparisons of metabolic parameters, in which the significance level was corrected by dividing 0.05 by the number of pairwise tests.

Results

Clinical characteristics

A total of 30 newly diagnosed stage IIIA–IV NSCLC patients were enrolled between September 2020 and August 2021. The clinical characteristics of 30 NSCLC patients are summarized in Table 1. Patients' median age at the time of diagnosis was 60 (range, 41–69) years. Among them, 27 (90%) patients were male and 3 (10%) were female. Besides, 27 (90%) and 3 (10%) patients had stage III and stage IV diseases, respectively. There were 16 (53.3%) patients with squamous cell carcinoma and 12 (40%) patients with adenocarcinoma. The mean value of FEV$_1$ for all patients was 2.3 L (range, 0.99–3.39).

Table 1 NSCLC patients' baseline characteristics ($n = 30$)

Characteristics	Number of patients (%)
Age, years old/median (range)	60 (41–69)
Gender	
Male	27 (90.0)
Female	3 (10.0)
ECOG	
0	9 (30.0)
1	21 (70.0)
Smoking status	
Yes	16 (53.3)
No	14 (46.7)
Tumor location	
Left upper	13 (43.3)
Left lower	3 (10.0)
Right upper	9 (30.0)
Right middle	1 (3.3)
Right lower	4 (13.3)
Histology	
Squamous cell carcinoma	16 (53.3)
Adenocarcinoma	12 (40.0)
Lymphoepithelioma-like carcinoma	1 (3.3)
NSCLC-NOS	1 (3.3)
Stage	
IIIA	5 (16.7)
IIIB	14 (46.7)
IIIC	8 (26.7)
IV	3 (9.9)
FEV$_1$, L	2.3 (0.99–3.39)

ECOG, Eastern Cooperative Oncology Group; *FEV$_1$*, forced expiratory volume in 1 s; *NSCLC*, non-small cell lung cancer; *NOS*, not specified

Unsupervised K-means classification of patients

The features used for patient classification were determined with the method of Laplacian feature importance scores (LSE). As shown in Fig. 1a, the Laplacian scores (LS) of all feature candidates were calculated and ranked in ascending order. Patlak-Ki and SUV$_{mean}$ of the PTs occupied the top 2 places, which indicated the highest importance for classification. The distance-based entropy (Fig. 1b) suggested that involving more features for classification based on the LS rank would generally decrease the stability and efficiency of the classification. The combination of Patlak-Ki and SUV$_{mean}$ of the PTs remained the best feature set for patient classification. Then, the number of patient clusters was determined through the silhouette analysis. As shown in Fig. 1c, the patient classification with 2 clusters showed the highest silhouette coefficient, which indicated that it was more appropriate to classify patients into 2 groups.
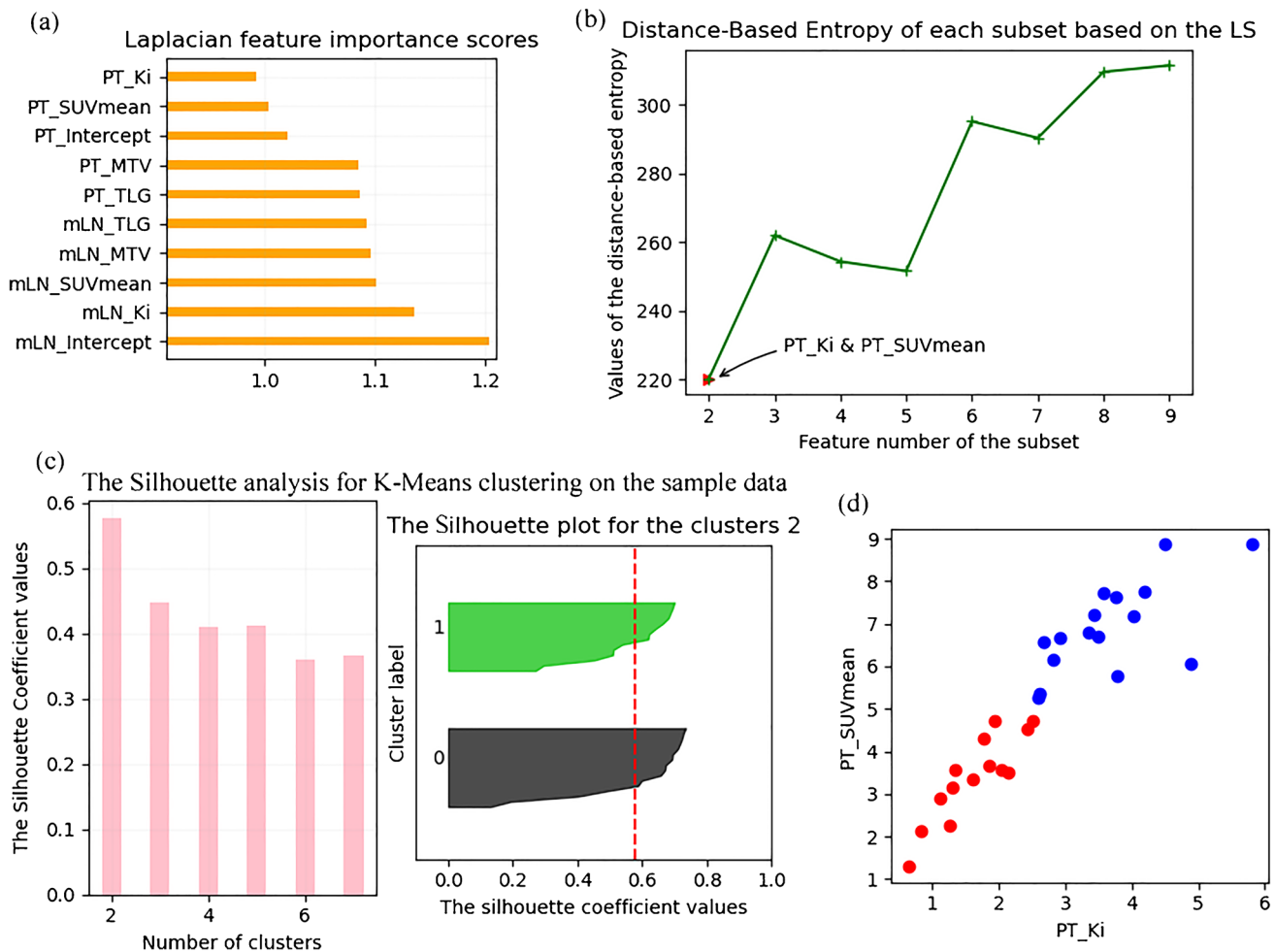
Fig. 1 Unsupervised classification of patients based on the PET parameters of PTs and mLNs. (**a**) The Laplacian scores (LS) of all feature candidates were calculated and ranked in ascending order. A smaller LS indicated that the feature was more important. (**b**) Distance-based entropy for the clusters with different feature subset, and the subset consists of the Ki and SUV$_{mean}$ showed the best performance. (**c**) The silhouette coefficient scores for the clusters with different number, and the patient classification with 2 clusters showed the highest silhouette coefficient values. (**d**) The visualization of the clustered data, where the blue points refer to the F-DFM group and the red points refer to the S-FDM group

Figure 1d illustrated the clustering results obtained from the K-means clustering. Among all the features, the Patlak-Ki and SUV$_{mean}$, rather than the volume-based metrics, contributed most to the grouping of the PTs. Therefore, the patients were divided into the fast dynamic FDG metabolism (F-DFM) group and the slow dynamic FDG metabolism (S-FDM) group based on Patlak-Ki and SUV$_{mean}$ of PTs.

Dynamic and static metabolic characterization of PTs

The PTs in the F-DFM group had significantly higher SUV$_{mean}$ (6.91 ± 1.09 g/ml vs. 3.40 ± 1.01 g/ml, $P < 0.001$) and Patlak-Ki (3.65 ± 0.89 ml/min/100 g vs. 1.63 ± 0.57 ml/min/100 g, $P < 0.001$) than those in the S-DFM group. However, no statistically significant differences were

observed between the F-DFM group and S-DFM group in terms of MTV [27.34 (range, 6.3–178.93) cm^3 vs. 52.97 (range, 1.43–159.12) cm^3, $P = 0.803$], TLG [214.17 (range, 48.06–1388.04) vs. 204.03 (range, 3.37–555.59), $P = 0.244$], and Patlak-Intercept (0.41 ± 0.19 vs. 0.39 ± 0.12, $P = 0.772$). The comparison of dynamic (Patlak-Ki and Patlak-Intercept) and static (SUV$_{mean}$, MTV, and TLG) metabolic characterization of the PTs is summarized in Fig. 2.

As shown in Fig. 3, different from PTs, no statistically significant differences were observed between the two groups regarding both Patlak-Ki and SUV$_{mean}$ of mLNs (Patlak-Ki of mLNs in the F-DFM and S-DFM groups: 1.96 ± 1.12 ml/min/100 g vs. 1.81 ± 1.00 ml/min/100 g, $P = 0.715$; SUV$_{mean}$ of mLNs in the F-DFM and S-DFM groups: 4.06 ± 2.00 g/ml vs. 3.80 ± 1.88 g/ml, $P = 0.719$). In the F-DFM group, the Patlak-Ki and SUV$_{mean}$ were significantly higher in PTs than
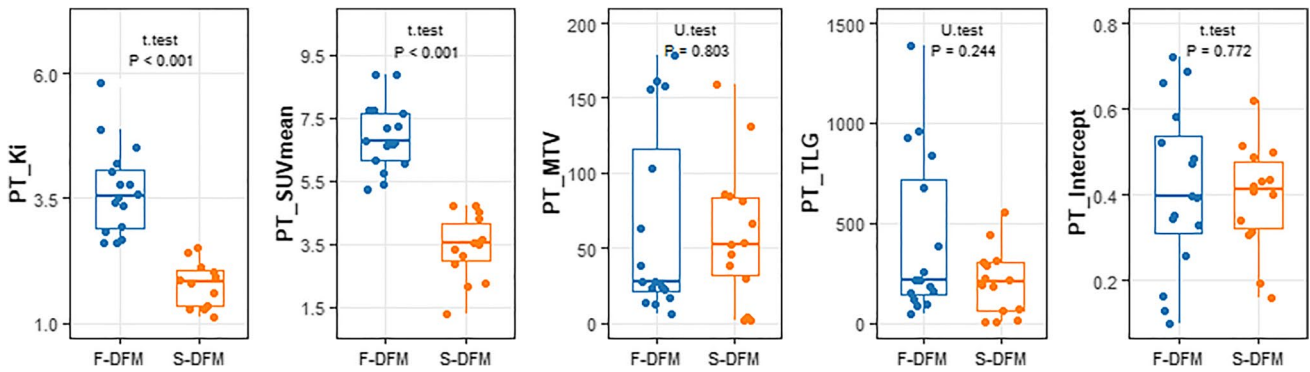
Fig. 2 The comparisons of Ki, SUV_{mean}, MTV, TLG, and intercept metrics for primary lung tumor (PT) between the F-DFM and S-DFM groups. The comparison of Ki, SUV_{mean}, and intercept was performed using the *t*-test, and the comparison of MTV and TLG was performed using the Mann–Whitney *U* test

Fig. 3 The comparisons of Ki and SUV_{mean} for primary lung tumor (PT) and metastatic lymph node (mLN) between the F-DFM and S-DFM groups. The *t*-test was used for each comparison; "***" indicates the $P < 0.001$, and "ns" indicates $P > 0.05$
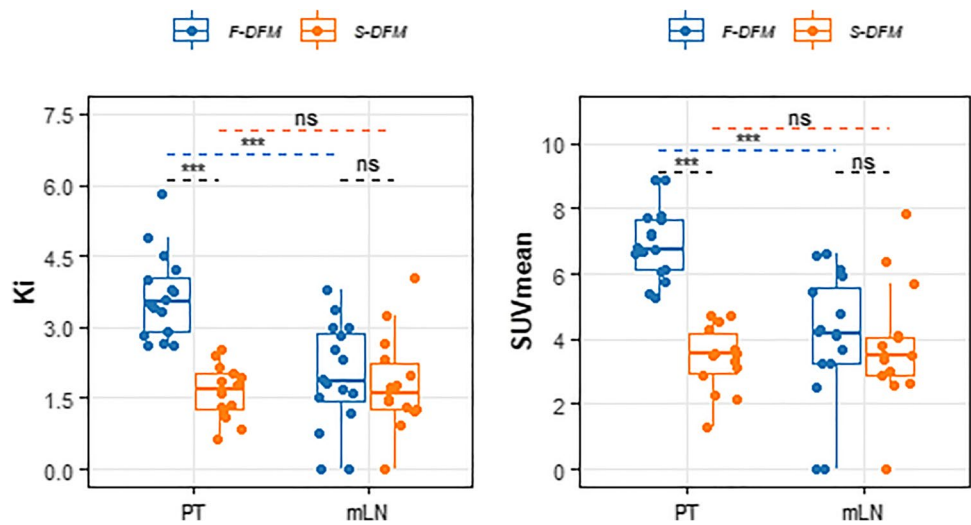
those in mLNs (Patlak-Ki of PTs and mLNs: 3.65 ± 0.89 ml/min/100 g vs. 1.96 ± 1.12 ml/min/100 g, $P < 0.001$; SUV_{mean} of PTs and mLNs: 6.91 ± 1.09 g/ml vs. 4.06 ± 2.00 g/ml, $P < 0.001$), which indicated higher metabolic activity of PTs. By contrast, there was no significant difference in metabolic activity of PTs and mLNs in the S-DFM group (Patlak-Ki of PTs and mLNs: 1.63 ± 0.57 ml/min/100 g vs. 1.81 ± 1.01 ml/min/100 g, $P = 0.556$; SUV_{mean} of PTs and mLNs: 3.40 ± 1.01 g/ml vs. 3.80 ± 1.88 g/ml, $P = 0.377$).

In the initial uptake time (0–3 min after [18F]FDG injection), all PTs and mLNs shared a tumor-like perfusion pattern (fast wash-in and washout). From 6 min after the [18F]FDG injection, PTs had faster and higher [18F]FDG uptake than mLNs in the F-DFM group, while no significant difference was observed in [18F]FDG uptake between PTs and mLNs in the S-DFM group. The dynamic FDG uptake of PTs in the F-DFM group was significantly different compared to that in the S-DFM group, while no significant difference was observed in the FDG uptake of mLNs between the two groups. Figures 4 and 5 display typical dynamic

[18F]FDG uptake patterns for patients in the F-DFM and S-DFM groups, respectively. It was revealed that PTs in the S-DFM group exhibited a more heterogeneous spatial distribution of FDG uptake than those in the F-DFM group.

The metabolic parameters of lesions were compared between the dynamic PET and the delayed static PET, and the results were shown in Fig. 6. The SUV_{mean} of PTs and mLNs derived from delayed static PET was remarkably linearly correlated with that from dynamic PET (PTs: $R^2 = 0.856$, $P < 0.001$; mLNs: $R^2 = 0.798$, $P < 0.001$). We also compared the SUV_{mean} of PTs assessed by the delayed PET between the F-DFM and S-DFM groups. The SUV_{mean} of PTs in the F-DFM group was statistically higher than that in the S-DFM group (9.94 ± 1.36 g/ml vs. 5.15 ± 1.89 g/ml, $P < 0.001$). No significant difference was observed in the SUV_{mean} of mLNs between the two groups (SUV_{mean} of mLNs in the F-DFM and S-DFM groups: 5.92 ± 2.68 g/ml vs. 5.3 ± 2.0 g/ml, $P = 0.508$).

A total of 51 textural features were extracted from PTs by 50–60-min PET imaging in the F-DFM and S-DFM groups.
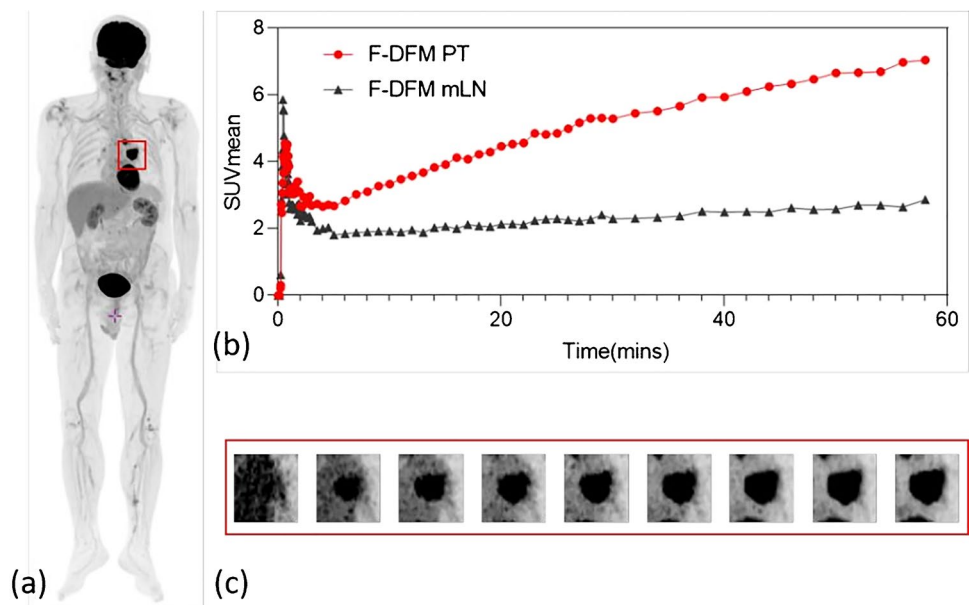
Fig. 4 The dynamic ^{18}F-FDG uptake patterns assessed by the 60-min dynamic total-body PET scan for an LA-NSCLC patient in the F-DFM group. (**a**) Maximum intensity projection (MIP) of the total-body ^{18}F-FDG PET of the patient in the F-DFM group. (**b**) Dynamic metabolic mean uptake curve for PTs (red) and mLNs (black) of the patient in the F-DFM group. (**c**) The snap MIP view of the dynamic ^{18}F-FDG uptake in PTs (red box) at 5 min, 9 min, 14 min, 19 min, 24 min, 29 min, 38 min, 48 min, and 58 min, respectively

Fig. 5 The dynamic ^{18}F-FDG uptake patterns assessed by the 60-min dynamic total-body PET scan for an LA-NSCLC patient in the S-DFM group. (**a**) Maximum intensity projection (MIP) of the total-body ^{18}F-FDG PET of the patient in the S-DFM group. (**b**) Dynamic metabolic mean uptake curve for PTs (red) and mLNs (black) of the patient in the S-DFM group. (**c**) The snap MIP view of the dynamic ^{18}F-FDG uptake in PTs (red box) at 5 min, 9 min, 14 min, 19 min, 24 min, 29 min, 38 min, 48 min, and 58 min, respectively
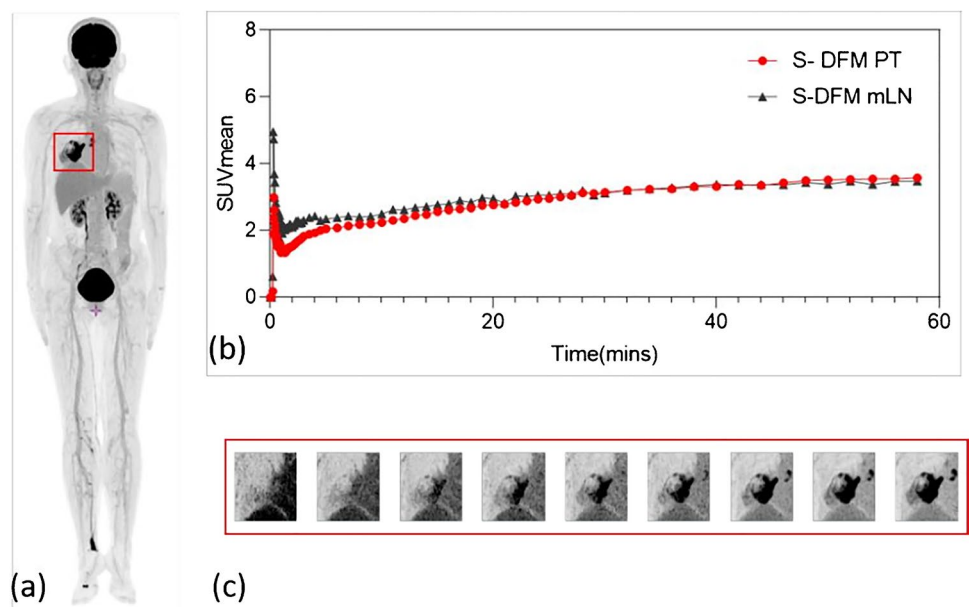
A significant difference was observed in textural patterns in PTs between the two groups (Supplementary Fig. 5). More specifically, PTs in the S-DFM group were more remarkably heterogeneous than those in the F-DFM group, and 9 of 13 heterogeneity-related features were significantly different between the two groups (Supplementary Fig. 6).

Gene profiling and IHC staining

The targeted NGS of PTs was performed in 12 patients, including 7 in the F-DFM group and 5 in the S-DFM group. The detailed genetic mutations of 12 patients were shown in Supplementary Fig. 7. TP53 and PI3KCA accounted for the most common mutated genes. The mean tumor mutational burden (TMB) was 8.4 mut/Mb for patients in the F-DFM group and 10.0 mut/Mb for those in the S-DFM group ($P = 0.715$).

The IHC staining of Ki67 (tumor cell proliferation), CD3$^+$ (T cell), CD8$^+$ (T cell), CD68$^+$ (macrophage), CD163$^+$ (macrophage), and CD34 (micro-vessel) was performed in PT tissues of 12 patients, including 6 patients in the F-DFM group and 6 patients in the S-DFM group (Figs. 7 and 8). The results revealed higher expressions of CD3$^+$(75.2% ± 10.1% vs. 38.7% ± 11.1%, $P < 0.001$), CD8$^+$ (72.0% ± 13.1% vs. 31.5% ± 7.1%, $P < 0.001$), CD68$^+$(55.0% ± 15.3% vs. 23.5% ± 10.0%, $P = 0.002$), and
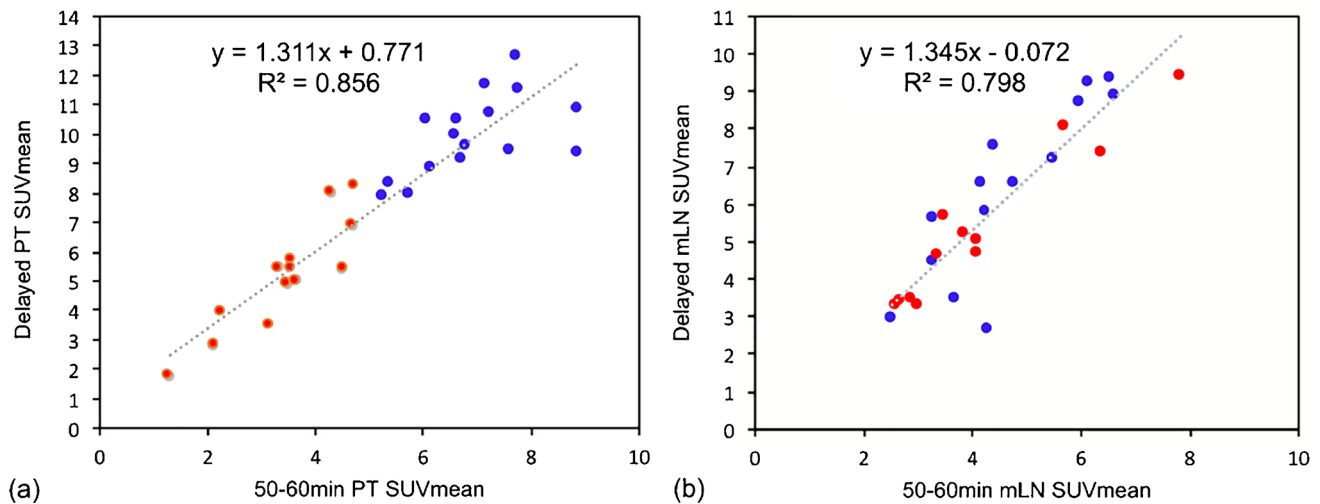
Fig. 6 The SUV_{mean} of PTs and mLNs derived from delayed static PET was remarkably linearly correlated with that from 50- to 60-min dynamic PET. [(**a**) PT, (**b**) mLN; blue points-F-DFM group, red points-S-DFM group]

$CD163^+$ ($62.8\% \pm 16.3\%$ vs. $28.7\% \pm 14.1\%$, $P = 0.003$) in the F-DFM group compared to the S-DFM group. The proliferative activity was examined by Ki67 ($58.7\% \pm 13.4\%$ vs. $53.5\% \pm 20.7\%$, $P = 0.619$), and MVD was assessed by CD34 ($35.7\% \pm 16.0\%$ vs. $37.5\% \pm 12.7\%$, $P = 0.831$), which were comparable between the two groups.

Discussion

The current study suggested that the pre-treatment dynamic total-body [18F]FDG PET/CT imaging could stratify NSCLC patients into the F-DFM and S-DFM groups, based on Patlak-Ki and SUV_{mean} of PTs. The PTs in the F-DFM group had significantly higher Patlak-Ki ($P < 0.001$) and SUV_{mean} ($P < 0.001$) than those in the S-DFM group. The texture analysis indicated that PTs in the S-DFM group were more heterogeneous than those in the F-DFM group. Higher T cells ($CD3^+/CD8^+$) and macrophages ($CD68^+/CD163^+$) infiltrations were observed in the F-DFM group. The study revealed the role of dynamic FDG uptake parameters in predicting the biological characteristics of NSCLC, supporting the hypothesis that total-body FDG PET/CT imaging could provide additional metabolic information for tumor heterogeneity evaluation and potentially guide risk stratification.

Cancer metabolism is profoundly different from normal cellular metabolism. The enhancement of glycolysis remains a cardinal metabolic alteration for tumor cells, and the excessive glucose uptake can be detected by the [18F]FDG PET [22]. Tumor metabolic heterogeneity could be regarded as a strong prognostic factor in different types of malignant tumors [23–26]. The current study indicated that PTs exhibited more significant heterogeneity in terms of dynamic glucose uptake compared with mLNs, which confirmed that the degree of glycolysis enhancement varied, even within tumor lesions in one patient. The primary tumor had a larger tumor burden with a more complex microenvironment than the metastatic lymph node, which might have contributed to its higher metabolic heterogeneity. A recent study examined the genomic landscape of 40 PTs and 61 metastatic tumors (MTs) by whole-exome sequencing and found that the concordance for the putative tumorigenic drivers was relatively high between PTs and MTs [27]. Of note, mLNs exhibited the lowest proportion of PTs-MTs shared alterations [27]. Jang et al. enrolled 52 patients with pharyngeal cancer who were treated with definitive chemoradiotherapy (CRT) [28]. The heterogeneity factor (HF) was defined as the derivative (dV/dT) of a volume-threshold function for PTs and mLNs. The results showed that HFs of PTs, rather than mLNs, were correlated with PET/CT parameters (MTV and TLG) and were predictive of response to radiotherapy and locoregional recurrence.

As we know, SUV is a simple semi-quantitative parameter for characterizing [18F]FDG uptake. Thus, the classification of patients solely based on SUV_{mean} might be less reliable compared with the combination of Patlak-Ki (an absolute quantification parameter) and SUV_{mean}. To compare the performance of two classification methods (SUV_{mean} vs. Patlak-Ki and SUV_{mean}), both SUV_{mean} derived from 40- to 60-min dynamic PET (SUV_{mean}-Dynamic) and SUV_{mean} from delayed static PET (SUV_{mean}-Delay) were calculated. The results indicated that the capacity to classify patients solely by SUV_{mean}-Dynamic/SUV_{mean}-Delay was reduced in certain cases sharing similar SUV values in the marginal area between the F-DFM and S-DFM groups (Supplementary
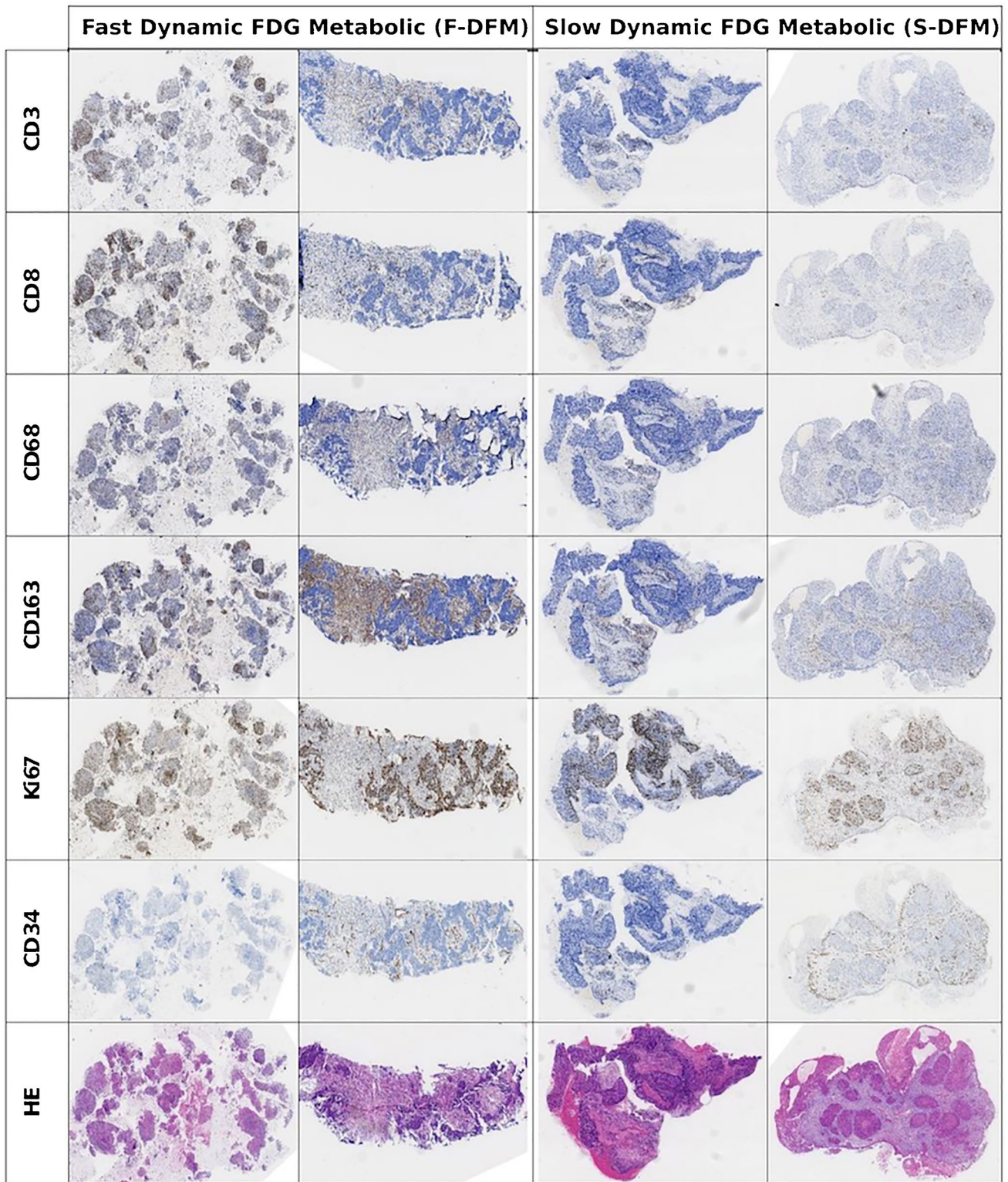
Fig. 7 The expressions of Ki67, CD3, CD8, CD34, CD68, and CD163 determined by immunohistochemistry (IHC) for primary tumors (PTs) in the F-DFM and S-DFM groups
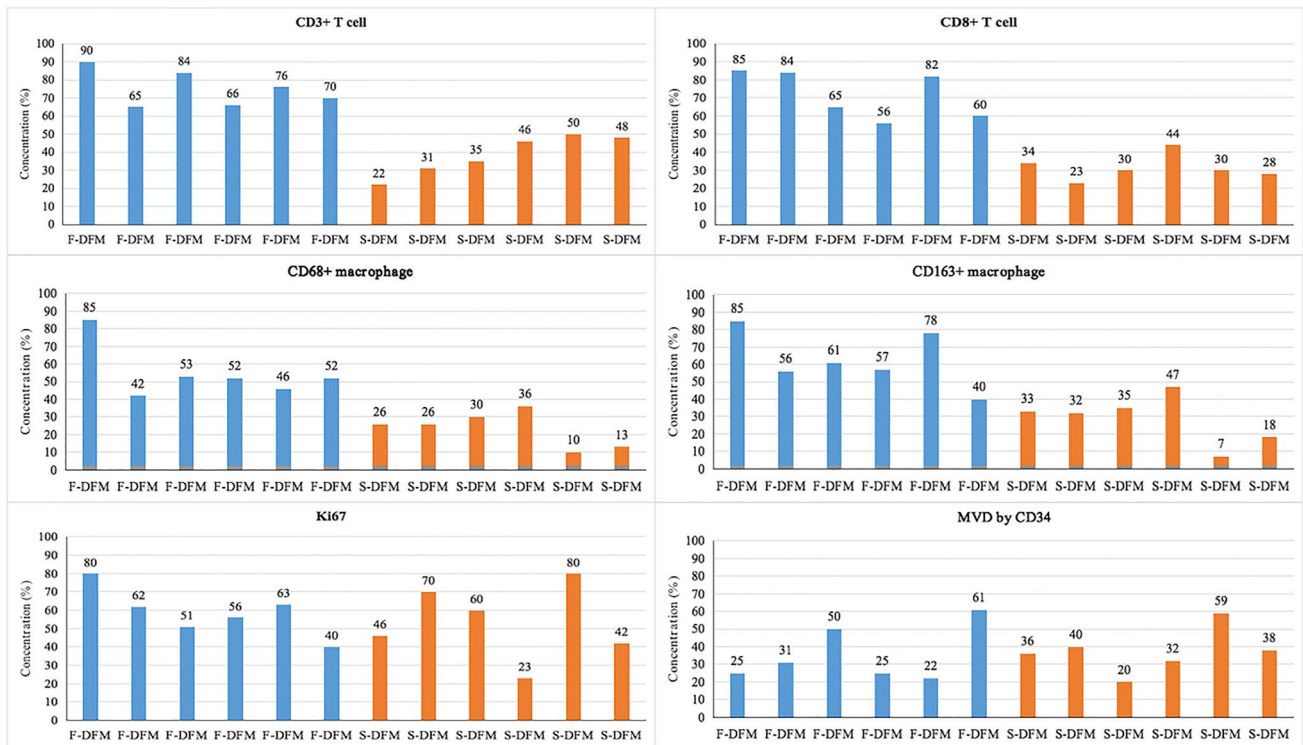
Fig. 8 The quantitation of Immunohistochemistry obtained by the image analysis for primary tumors (PTs) in 12 patients (6 patients in the F-DFM group vs. 6 patients in the S-DFM group). The results revealed higher expressions of CD3^{+}, CD8^{+}, CD68^{+}, and CD163^{+} in the F-DFM group

Fig. 8). By contrast, a clear boundary could be obtained between the F-DFM and S-DFM groups when combining Ki and SUV_{mean}-Dynamic, which demonstrated the advantage of dynamic PET parameters in stratifying patients. The delayed static PET imaging did not provide enough information to differentiate patients between the F-DFM and S-DFM groups.

The higher Patlak-Ki and SUV_{mean} of PTs were observed in the F-DFM group, which indicated the higher capability of [^{18}F]FDG uptake over time. The tumor metabolic characteristics examined by dynamic total-body PET could be different at the single-cell level, which might be influenced by the genetic background of tumor cells and the tumor microenvironment (TME) [29]. A recent study reported that diverse cell populations preferentially acquired distinct metabolites from a common pool of metabolites in the TME [30]. A significantly higher amount of glucose was consumed by tumor myeloid cells over tumor-infiltrating T cells or cancer cells on a per-cell basis, and tumor-infiltrating immune cells were more active than those in the spleen [30]. Their results also suggested that glucose was not broadly limited and the TME-resident cells were capable of increasing glucose uptake in vivo when glutamine uptake was restricted [30]. Immune cells preferentially consumed a noticeably higher amount of glucose than cancer cells.

In this study, we examined the expressions of tumor-infiltrating T cells and macrophages of PTs using IHC. The results indicated that the F-DFM group had higher expressions of CD3^{+}/CD8^{+} T cells and CD68^{+}/CD163^{+} macrophages than the S-DFM group, while Ki67 expression was comparable between the two groups. Hence, the higher values of SUV_{mean} and Patlak-Ki in the F-DFM group might result from the higher infiltrations of T cells (CD3^{+}/CD8^{+}) and macrophages (CD68^{+}/CD163^{+}) in the TME. In addition to TMB and PD-L1, multiple types of immune cells have been evaluated to predict the treatment response to immune checkpoint inhibitor (ICI) therapy in NSCLC [31–33]. The CD8^{+} T cell infiltration was reported to be associated with the efficacy of ICI therapy [31, 34–36]. Liu et al. revealed an association between high levels of CD68^{+}PD-L1^{+} macrophages and improved overall survival (OS) in NSCLC patients who were treated with ICI therapy [37]. Our findings suggested that dynamic FDG PET could provide particular FDG metabolic information of TME, and F-DFM NSCLC patients might benefit from ICI therapy due to the high infiltrations of immune cells. In this sense, the dynamic FDG PET could be helpful for treatment decision-making and clinical trial design in NSCLC.

The genetic properties of tumors determined the aggressiveness and growth pattern, which might influence

the FDG uptake ability of tumor cells. The relationship between static PET parameters and tumor genetic heterogeneity has been explored, but the results remained controversial [38–41]. In several studies, no correlation was observed between PET parameters and TMB in NSCLC [40, 41]. Our study evaluated the association of dynamic FDG uptake characteristics with gene mutation patterns and TMB, and no significant correlation was found.

There were two reasons why the delayed static PET scan was performed in this study. Firstly, in previous studies which involved conventional PET, the addition of delayed PET was reported to raise the accuracy of diagnosis of metastases and staging of mediastinal node in patients with lung cancer [42, 43]. We assumed that the delayed static PET scan might be helpful in the detection of distant metastatic lesions in unresectable NSCLC patients. Secondly, we attempted to compare the metabolic characteristics of lesions between the dynamic PET and the delayed static PET, with the aim of exploring additional information for tumor heterogeneity evaluation. No additional metastatic lesions were detected with the delayed static PET imaging in this study. The results showed that the SUV_{mean} of PTs and mLNs derived from delayed static PET was remarkably linearly correlated with that from dynamic PET, which suggested that the delayed static PET did not provide additional metabolic information. Based on the results, the PET scan protocol would be optimized in subsequent studies.

There are some limitations to this work. First, only 30 patients could be enrolled in the present study, and the results should be validated by a study with a larger sample size. Second, the amount of biopsy tissue samples might be insufficient, and the quality might not be high enough for pathological and molecular testing. IHC analysis was performed in only 12 PT samples in the current study, and the differences between samples from PTs and mLNs were unable to be compared. Genetic testing was performed on only 12 patients; thus, the correlation between dynamic FDG PET and genetic properties should be further validated. Third, the association of Patlak-Ki and immune cells infiltration ($CD3^+$/$CD8^+$ T cells and $CD68^+$/$CD163^+$ macrophages of PTs) with treatment outcomes needs to be explored in the future. Despite these limitations, the current study made a comprehensive description of the dynamic FDG uptake patterns of PTs and mLNs by the dynamic total-body PET, which could be helpful for a deeper insight into tumor heterogeneity. The correlation between dynamic FDG-uptake parameters and treatment response to ICI therapy will be reported in an observational study (NCT04654234) when the median follow-up time reaches 12 months.

Conclusions

The dynamic total-body [^{18}F]FDG PET/CT stratified NSCLC patients into the F-DFM and S-DFM groups, based on Patlak-Ki and SUV_{mean} of PTs. PTs in the F-DFM group seemed to be more homogenous in terms of the [^{18}F]FDG uptake than those in the S-DFM group, with higher SUV_{mean} and Patlak-Ki. The higher infiltrations of T cells and macrophages were observed in the PTs for the F-DFM group, which suggested a potential benefit from immunotherapy.

Declarations

References

1. Testa, U., G. Castelli, and E. Pelosi, Lung cancers: molecular characterization, clonal heterogeneity and evolution, and cancer stem cells. Cancers (Basel), 2018;10(8).
2. Voigt W, et al. Beyond tissue biopsy: a diagnostic framework to address tumor heterogeneity in lung cancer. Curr Opin Oncol. 2020;32(1):68–77.
3. Yoon SH, et al. Tumor heterogeneity in lung cancer: assessment with dynamic contrast-enhanced MR imaging. Radiology. 2016;280(3):940–8.
4. Lee WC, et al. Multiregion gene expression profiling reveals heterogeneity in molecular subtypes and immunotherapy response signatures in lung cancer. Mod Pathol. 2018;31(6):947–55.
5. Katiyar P, et al. Spectral clustering predicts tumor tissue heterogeneity using dynamic (18)F-FDG PET: a complement to

the standard compartmental modeling approach. J Nucl Med. 2017;58(4):651–7.

6. Tixier F, et al. Visual versus quantitative assessment of intratumor 18F-FDG PET uptake heterogeneity: prognostic value in non-small cell lung cancer. J Nucl Med. 2014;55(8):1235–41.

7. Markovina S, et al. Regional lymph node uptake of [(18)F]fluorodeoxyglucose after definitive chemoradiation therapy predicts local-regional failure of locally advanced non-small cell lung cancer: results of ACRIN 6668/RTOG 0235. Int J Radiat Oncol Biol Phys. 2015;93(3):597–605.

8. Hyun SH, et al. Intratumoral heterogeneity of (18)F-FDG uptake predicts survival in patients with pancreatic ductal adenocarcinoma. Eur J Nucl Med Mol Imaging. 2016;43(8):1461–8.

9. Sanli, Y., et al.,2019 Tumor heterogeneity on FDG PET/CT and immunotherapy: an imaging biomarker for predicting treatment response in patients with metastatic melanoma. AJR Am J Roentgenol, p. 1–9.

10. Kaira K, et al. Metabolic activity by (18)F-FDG-PET/CT is predictive of early response after nivolumab in previously treated NSCLC. Eur J Nucl Med Mol Imaging. 2018;45(1):56–66.

11. Cook GJ, et al. Are pretreatment 18F-FDG PET tumor textural features in non-small cell lung cancer associated with response and survival after chemoradiotherapy? J Nucl Med. 2013;54(1):19–26.

12. Krarup MMK, et al. Heterogeneity in tumours: validating the use of radiomic features on (18)F-FDG PET/CT scans of lung cancer patients as a prognostic tool. Radiother Oncol. 2020;144:72–8.

13. Nakajo M, et al. Texture analysis of (18)F-FDG PET/CT to predict tumour response and prognosis of patients with esophageal cancer treated by chemoradiotherapy. Eur J Nucl Med Mol Imaging. 2017;44(2):206–14.

14. Moscoso A, et al. Texture analysis of high-resolution dedicated breast (18) F-FDG PET images correlates with immunohistochemical factors and subtype of breast cancer. Eur J Nucl Med Mol Imaging. 2018;45(2):196–206.

15. Cheng NM, et al. Prognostic value of tumor heterogeneity and SUVmax of pretreatment 18F-FDG PET/CT for salivary gland carcinoma with high-risk histology. Clin Nucl Med. 2019;44(5):351–8.

16. Cherry SR, et al. Total-body PET: maximizing sensitivity to create new opportunities for clinical research and patient care. J Nucl Med. 2018;59(1):3–12.

17. Zhang YQ, et al. The image quality, lesion detectability, and acquisition time of (18)F-FDG total-body PET/CT in oncological patients. Eur J Nucl Med Mol Imaging. 2020;47(11):2507–15.

18. Zhang X, et al. Total-body dynamic reconstruction and parametric imaging on the uEXPLORER. J Nucl Med. 2020;61(2):285–91.

19. Silvestri GA, et al. Methods for staging non-small cell lung cancer: diagnosis and management of lung cancer, 3rd ed: American College of Chest Physicians evidence-based clinical practice guidelines. Chest. 2013;143(5 Suppl):e211S-e250S.

20. Hellwig D, et al. 18F-FDG PET for mediastinal staging of lung cancer: which SUV threshold makes sense? J Nucl Med. 2007;48(11):1761–6.

21. Liu R, et al. An unsupervised feature selection algorithm: Laplacian score combined with distance-based entropy measure. IEEE. 2009;3:65–8.

22. Upadhyay M, et al. The Warburg effect: insights from the past decade. Pharmacol Ther. 2013;137(3):318–30.

23. Pinho DF, et al. Value of intratumoral metabolic heterogeneity and quantitative (18)F-FDG PET/CT parameters in predicting prognosis for patients with cervical cancer. AJR Am J Roentgenol. 2020;214(4):908–16.

24. Mena E, et al. Value of intratumoral metabolic heterogeneity and quantitative 18F-FDG PET/CT Parameters to predict prognosis in patients with HPV-positive primary oropharyngeal squamous cell carcinoma. Clin Nucl Med. 2017;42(5):e227–34.

25. Hatt M, et al. Robustness of intratumour (1)(8)F-FDG PET uptake heterogeneity quantification for therapy response prediction in oesophageal carcinoma. Eur J Nucl Med Mol Imaging. 2013;40(11):1662–71.

26. Kim DH, et al. Quantification of intratumoral metabolic macroheterogeneity on 18F-FDG PET/CT and its prognostic significance in pathologic N0 Squamous cell lung carcinoma. Clin Nucl Med. 2016;41(2):e70–5.

27. Tang WF, et al. Timing and origins of local and distant metastases in lung cancer. J Thorac Oncol. 2021;16(7):1136–48.

28. Jang JY, et al. Differential prognostic value of metabolic heterogeneity of primary tumor and metastatic lymph nodes in patients with pharyngeal cancer. anticancer Res. 2017;37(10):5899–905.

29. Xiao Z, Dai Z, Locasale JW. Metabolic landscape of the tumor microenvironment at single cell resolution. Nat Commun. 2019;10(1):3763.

30. Reinfeld BI, et al. Cell-programmed nutrient partitioning in the tumour microenvironment. Nature. 2021;593(7858):282–8.

31. Haratani K, et al. Tumor immune microenvironment and nivolumab efficacy in EGFR mutation-positive non-small-cell lung cancer based on T790M status after disease progression during EGFR-TKI treatment. Ann Oncol. 2017;28(7):1532–9.

32. Thommen DS, et al. A transcriptionally and functionally distinct PD-1(+) CD8(+) T cell pool with predictive potential in non-small-cell lung cancer treated with PD-1 blockade. Nat Med. 2018;24(7):994–1004.

33. Althammer S, et al. Automated image analysis of NSCLC biopsies to predict response to anti-PD-L1 therapy. J Immunother Cancer. 2019;7(1):121.

34. Schmid P, et al. Pembrolizumab plus chemotherapy as neoadjuvant treatment of high-risk, early-stage triple-negative breast cancer: results from the phase 1b open-label, multicohort KEYNOTE-173 study. Ann Oncol. 2020;31(5):569–81.

35. Chen Y, et al. The frequency and inter-relationship of PD-L1 expression and tumour mutational burden across multiple types of advanced solid tumours in China. Exp Hematol Oncol. 2020;9:17.

36. Ji S, et al. Peripheral cytokine levels as predictive biomarkers of benefit from immune checkpoint inhibitors in cancer therapy. Biomed Pharmacother. 2020;129:110457.

37. Liu Y, et al. Immune cell PD-L1 colocalizes with macrophages and is associated with outcome in PD-1 pathway blockade therapy. Clin Cancer Res. 2020;26(4):970–7.

38. Nair VS, et al. Prognostic PET 18F-FDG uptake imaging features are associated with major oncogenomic alterations in patients with resected non-small cell lung cancer. Cancer Res. 2012;72(15):3725–34.

39. Ono A, et al. Assessment of associations between clinical and immune microenvironmental factors and tumor mutation burden in resected nonsmall cell lung cancer by applying machine learning to whole-slide images. Cancer Med. 2020;9(13):4864–75.

40. Moon SH, et al. Correlations between metabolic texture features, genetic heterogeneity, and mutation burden in patients with lung cancer. Eur J Nucl Med Mol Imaging. 2019;46(2):446–54.

41. Kim BS, et al. Association between immunotherapy biomarkers and glucose metabolism from F-18 FDG PET. Eur Rev Med Pharmacol Sci. 2020;24(16):8288–95.

42. Uesaka D, et al. Evaluation of dual-time-point 18F-FDG PET for staging in patients with lung cancer. J Nucl Med. 2008;49(10):1606–12.

43. Hu M, et al. Value of dual-time-point FDG PET/CT for mediastinal nodal staging in non-small-cell lung cancer patients with lung comorbidity. Clin Nucl Med. 2011;36(6):429–33.

Authors and Affiliations

DaQuan Wang[1] · Xu Zhang[2] · Hui Liu[3] · Bo Qiu[1] · SongRan Liu[4] · ChaoJie Zheng[3] · Jia Fu[4] · YiWen Mo[2] · NaiBin Chen[1] · Rui Zhou[1] · Chu Chu[1] · FangJie Liu[1] · JinYu Guo[1] · Yin Zhou[5] · Yun Zhou[3] · Wei Fan[2] · Hui Liu[1]

[1] Department of Radiation Oncology, State Key Laboratory of Oncology in South China, Collaborative Innovation Center of Cancer Medicine, Sun Yat-Sen University Cancer Center, Guangzhou 510060, China

[2] Department of Nuclear Medicine, State Key Laboratory of Oncology in South China, Collaborative Innovation Center of Cancer Medicine, Sun Yat-Sen University Cancer Center, Guangzhou 510060, China

[3] United Imaging Healthcare, Shanghai, China

[4] Department of Pathology, State Key Laboratory of Oncology in South China, Collaborative Innovation Center of Cancer Medicine, Sun Yat-Sen University Cancer Center, Guangzhou 510060, China

[5] SuZhou TongDiao Company, Suzhou, China